Insights on earthquake triggering processes from early aftershocks of repeating microearthquakes

Olivier Lengliné, Jean-Paul Ampuero

▶ To cite this version:

Olivier Lengliné, Jean-Paul Ampuero. Insights on earthquake triggering processes from early aftershocks of repeating microearthquakes. Journal of Geophysical Research, 2015, 10.1002/2015JB012287 . hal-01214186

HAL Id: hal-01214186
https://hal.science/hal-01214186

Submitted on 12 Oct 2015

HAL is a multi-disciplinary open access archive for the deposit and dissemination of scientific research documents, whether they are published or not. The documents may come from teaching and research institutions in France or abroad, or from public or private research centers.

L'archive ouverte pluridisciplinaire **HAL**, est destinée au dépôt et à la diffusion de documents scientifiques de niveau recherche, publiés ou non, émanant des établissements d'enseignement et de recherche français ou étrangers, des laboratoires publics ou privés.

JOURNAL OF GEOPHYSICAL RESEARCH, VOL. ???, XXXX, DOI:10.1002/,

Insights on Earthquake Triggering Processes from Early Aftershocks of Repeating Micro-Earthquakes

O. Lengliné[1] and J.-P. Ampuero[1]

O. Lengliné, Institut de Physique du Globe de Strasbourg, Ecole et Observatoire des Sciences de la Terre, 5 rue René Descartes, 67084 Strasbourg cedex, France. (lengline@unistra.fr)

J. P. Ampuero, Seismological Laboratory, California Institute of Technology, 1200 E. California Blvd, Pasadena, CA 91125, USA. (ampuero@gps.caltech.edu)

[1]Seismological Laboratory, California
Institute of Technology, Pasadena, USA

Abstract. Characterizing the evolution of seismicity rate of early aftershocks can yield important information about earthquake nucleation and triggering. However, this task is challenging because early aftershock seismic signals are obscured by those of the mainshock. Previous studies of early aftershocks employed high-pass filtering and template matching, but had limited performance and completeness at very short times. Here we take advantage of repeating events previously identified on the San Andreas fault at Parkfield and apply empirical Green's function deconvolution techniques. Both Landweber and sparse deconvolution methods reveal the occurrence of aftershocks as early as few tenths of a second after the mainshock. These events occur close to their mainshock, within one to two rupture lengths away. The aftershock rate derived from this enhanced catalog is consistent with Omori's law, with no flattening of the aftershock rate down to the shortest resolvable time scale ~ 0.3 s. The early aftershock rate decay determined here matches seamlessly the decay at later times derived from the original earthquake catalog, yielding a continuous aftershock decay over time scales spanning nearly 8 orders of magnitude. Aftershocks of repeating micro-earthquakes may hence be governed by the same mechanisms from the earliest time resolved here, up to the end of the aftershock sequence. Our results suggest that these early aftershocks are triggered by relatively large stress perturbations, possibly induced by aseismic afterslip with very short characteristic time. Consistent with previous observations on bimaterial faults, the relative location of early aftershocks shows asymmetry along-strike, persistent over long periods.

1. Introduction

Earthquake aftershock sequences are one of the most abundant manifestations of seismic activity and earthquake interactions. A robust characteristic is that their seismicity rate, $\lambda(t)$, decays as a function of time t after the mainshock as a power-law well described by the Omori-Utsu law [*Utsu et al.*, 1995],

$$\lambda(t) = K/(t+c)^p. \tag{1}$$

where the exponent p is usually ~ 1, the aftershock productivity K generally depends on mainshock magnitude, and the time scale c marks the onset of the power-law regime. Despite the robustness of this empirical observation, the detailed mechanism responsible for aftershock sequences is still elusive and represents a major challenge for understanding the physics of earthquake nucleation and triggering. Several seismicity models, invoking very different physical mechanisms, have been equally successful at explaining the power-law decay of aftershock rates. These include rate-and-state nucleation models driven by static stress transfer from the mainshock [*Dieterich*, 1994], Coulomb earthquake triggering models driven by postseismic slip [e.g. *Schaff et al.*, 1998] or by pore fluid diffusion and poroelastic stress transfer [e.g. *Bosl and Nur*, 2002], and mechanisms triggered by dynamic stresses carried by the mainshock wavefield such as modifications of the fault zone properties [e.g. *Parsons*, 2005] and aseismic slip transients [e.g. *Shelly et al.*, 2011]. Hence the power-law regime of aftershock decay rates contains limited information to discriminate among earthquake triggering models. However, at early times after the mainshock the predictions of aftershock models diverge [e.g. *Helmstetter and Shaw*, 2009], suggesting that quantification of early aftershock rates can provide constraints on the physical mechanism. This task is non-trivial because analysis of early aftershock signals is severely obstructed by the coda of the mainshock. It is not yet clear if the characteristic time c in Eq. 1 has a physical origin [e.g. *Dieterich*, 1994; *Narteau et al.*, 2009] or mainly results from observational bias [*Kagan*, 2004; *Kagan and Houston*, 2005; *Helmstetter et al.*, 2006]. Indeed, incompleteness of earthquake catalogs at early times produces an apparent saturation of the earthquake rate right after the mainshock.

Previous efforts to detect early aftershocks involved either amplitude-threshold detectors on high-pass filtered waveform envelopes [e.g. *Peng et al.*, 2006, 2007; *Enescu et al.*, 2007, 2009] or matched filter detectors [e.g. *Peng and Zhao*, 2009; *Lengliné et al.*, 2012]. Most of these studies recover a large number of early aftershocks and show an apparent decrease of aftershock rate at early times. However, the completeness achieved by these methods soon after the mainshock is much poorer than at later times, hampering the quantitative analysis of aftershock decay rates over a broad time scale range. *Enescu et al.* [2009] inferred, from the study of early aftershocks of relatively large earthquakes, c-values on the order of their lowest resolvable time scale $\sim$ 1 min. Hence no flattening of the Omori decay was observed and the c-value could be even smaller. *Sawazaki and Enescu* [2014] found a transition of aftershock rate behavior between 10 and 40 s after a Mw6.9 earthquake and attributed it to the transition between the dynamic and static triggering regimes.

Here we propose a novel strategy to quantify early aftershock activity. We consider a composite aftershock sequence obtained by stacking multiple sequences relative to mainshock time and location. We focus on earthquakes with very similar waveforms, which facilitates the uniform detection of aftershocks within their mainshock's coda. We present two deconvolution approaches which capture aftershocks in the first 20 s following a mainshock. We show that we can detect events as early as 0.3 s after their mainshock, that is, a time scale of about ten times the mainshock rupture duration. Comparing aftershock rates in our newly identified events with those at later times, we find a constant power-law decay of the aftershock rate from the earliest resolvable time (0.3 s) up to about 100 days. Our results suggest that the mechanism driving aftershock activity remains similar over a broad range of time scales spanning 8 orders of magnitude.

2. Data

We used the repeating earthquake catalog of *Lengliné and Marsan* [2009], which comprises events with magnitudes ranging from $M_L = 0.9$ to $M_L = 3.2$ that occurred between 1984 and June 2007. This dataset contains 2414 events distributed in 334 repeating earthquake sequences (RES) formed by linking earthquake pairs with similar waveforms, overlapping source areas and similar magnitudes (see details in *Lengliné and Marsan* [2009]). The dataset is provided in the supplementary material. The analysis is based on waveforms recorded by the short-period vertical sensors of the Northern California Seismic Network (NCSN) (Figure 1). We selected 20.48 s long signal segments, sampled at 100 Hz (2048 samples), starting 1 s before the P-wave arrival. We used all NCSN stations with at least one phase pick for the earthquakes considered here. We used all available records at these NSCN stations to form the dataset. For reference, 12 out of these 396 stations recorded half of the events; they are located at less than 20 km from the event epicenters.

3. Methods

3.1. Deconvolution of Repeating Earthquake Signals

Identifying the seismic signature of very early aftershocks is not straightforward, because it overlaps with the coda waves of the mainshock (Figure 3). For instance, a template matching approach has limited detection capacity on such early signals (see Appendix A). Here we propose a deconvolution method for reliable early aftershock detection. Previous related work includes *Fischer* [2005] and *Wang et al.* [2014]. Our analysis focuses on nearby events and exploits waveform similarity to facilitate the search. We note $u_i^k(t)$ the waveform of the i^{th} event of a given sequence recorded at station k. In the Fraunhofer approximation, this waveform can be represented as the temporal convolution ($*$) between the apparent source time function (ASTF), $f_i^k(t)$, which depends on the source-receiver configuration, and a Green's function, $G_i^k(t)$, that incorporates all effects related to seismic wave propagation and instrument response:

$$u_i^k(t) = [G_i^k * f_i^k](t) \doteq \int_{-\infty}^{+\infty} G_i^k(t-t') f_i^k(t') dt'. \tag{2}$$

Our first objective is to recover $f_i^k(t)$ by deconvolution. The source time functions will then be analyzed to identify if any aftershock occurs during the 20.48 s long time window studied. The deconvolution process is based on empirical Green's functions (EGF), i.e. the waveform of an earthquake located close to earthquake i and recorded at the same station k, such that the nearly common ray paths for the two earthquakes implies a similar G_i^k. The ASTFs obtained by EGF deconvolution are not absolute, but relative to the ASTFs of the EGF event. We denote the resulting relative source time function as RSTF. In studies addressing in detail the rupture process of a target earthquake i, the EGF is chosen as a significantly smaller event to allow a point-source approximation. In contrast, our goal here is to detect secondary events in the wake of earthquake i which is part of a RES, without attempting to resolve their individual rupture process. We hence choose as EGF event another earthquake of the RES. As all events in a RES have very similar magnitudes, their individual source time functions are very similar. Hence, if no aftershock occurs during the investigated time window the RSTF should be a single Dirac delta function. If an aftershock sufficiently similar (located closely) to the other events of the RES occurs, another peak should emerge in the RSTF (Figure 4).

To retrieve the RSTFs we apply the projected Landweber deconvolution algorithm [e.g. *Piana and Bertero*, 1997; *Bertero et al.*, 1997; *Vallée*, 2004]. This deconvolution procedure is an iterative process and we set $f = 0$ as a starting guess. The target waveform, $u_i^k(t)$, and the EGF waveform, $u_j^k(t)$, are aligned to the nearest sample based on the time shift of the maximum of their cross-correlation function. If the normalized cross-correlation of the entire 20.48 s of signals is higher than 0.7, we proceed with the deconvolution process. This criterion is fulfilled by most of the earthquake pairs we considered, because events in a RES have very similar waveforms by definition. The purpose of this step is to remove stations with very noisy signals that produce poor reconstruction of the RSTF.

We assess through simulations whether this selection criterion excludes waveforms with shortly separated earthquake doublets that may have low correlation coefficient due to destructive interference. We build a synthetic doublet waveform as the sum of the original waveform and a shifted version of it. We then compute the correlation coefficient between the original and the synthetic doublet waveform. We test each possible time shift and repeat this operation for a random set of 100 events in our catalogue at all possible stations. We find that the correlation coefficient is higher than 0.7 if the second event occurs after more than 0.3 s (Figure 2). At shorter inter-event times the correlation coefficient falls from 1.0 at zero inter-event time to around 0.65 at an inter-event time of 0.1 s. In reality, the correlation coefficient is higher than in these synthetics because aftershocks are usually smaller than their mainshock, hence produce less interference. Our selection criterion thus may exclude aftershocks at times shorter than 0.3 s. However, as shown later, the deconvolution results are quite noisy in the first 0.3 s anyway. Hence, this selection step does not limit the aftershock detection capability, it simply removes noisy waveforms.

The waveform u is filtered with a 4th-order Butterworth low-pass filter with cut-off frequency of 20 Hz. This stabilizes the deconvolution procedure, yielding less noisy RSTFs. At each iteration we estimate

$$f_{n+1} = \mathcal{P}\left[f_n + \tau G^{\mathrm{T}} * (u - G * f_n)\right] \tag{3}$$

where f_n is the RSTF estimated at iteration n, $\mathcal{P}$ a projection operator, G the EGF, G^{T} its transpose, and τ is a relaxation parameter. Following *Vallée* [2004], we set $\tau = 1/(\max_\omega |\hat{G}(\omega)|^2)$, where $\hat{G}$ is the Fourier transform of G and ω is frequency. The projection operator $\mathcal{P}$ is defined as follows:

$$\mathcal{P}f(t) = \begin{cases} f(t) & \text{if } f(t) > 0 \text{ and } 0 < t < T \\ 0 & \text{elsewhere} \end{cases} \tag{4}$$

This imposes two constraints on $f(t)$, positivity and an upper bound on its duration (T=20 s). The latter is mostly to prevent spurious values at the end of the time interval where data constraints are weak. The iteration process stops either when we reach a maximum number of allowed iterations or when the residual, $\varepsilon = \parallel u - G * f \parallel_2$ does not decrease significantly any more. Once convergence is reached, we normalize f by its maximum amplitude. We then stack RSTFs computed from all EGFs, at all stations (Figure 5). By stacking RSTFs obtained at different stations we focus on aftershocks located close to their mainshock, otherwise stacking would not result in constructive interference. This is also consistent with the fact that our analysis relies on waveform similarity. The final product is, for each event in the original catalog, a source time function (STF) that can reveal the occurrence of similar events in the first ~ 20 s.

3.2. Identifying Early Aftershocks

Our next objective is to identify if aftershocks occurred during the investigated time period, i.e. in the first 19.48 s after the mainshock. We scan through the stacked STF for prominent peaks. We first remove from the STF any long period trend. As the noise level might vary across the whole duration of the STF, we proceed to the detection of peaks in consecutive windows of 1 s. For each window we compute the mean μ and standard deviation σ of the STF function. If a peak (local maximum) is higher than $\mu + 5\sigma$ we keep it as a possible detection. We declare a detection if the peak is the largest one (excluding the first peak corresponding to the mainshock). We only found 1 instance of multiple aftershocks in our dataset. Following this procedure, we identified 68 early aftershocks out of 2414 events in the dataset. Repeating the same operation with a different threshold setting, $m + 9MAD$ where m is the median and MAD the median absolute deviation of the STF within the 1 s window, we identify 78 early aftershocks. A total of 64 events with early aftershocks are identified in common by both criteria. The remaining events have large noise, so we exclude them from our further analysis.

3.3. Verifying the Identification of Early Aftershocks

Although the waveforms considered here are very similar and tend to produce stable deconvolution results, in some instances the deconvolution process leads to noisy RSTFs, making it difficult to distinguish if a peak is significant. In order to assess the robustness of our RSTFs, we test a second deconvolution technique on the 64 events identified above. As we expect only few aftershocks in the first 20 s, most of the RSTF values should be null. We hence employ a sparse deconvolution procedure that favors RSTFs with a low number of non-zero values, following a formulation similar to *Rodriguez et al.* [2012]. We assume that the target waveform $\mathbf{u}$ can be written as a linear combination of a subset of the waveforms $\boldsymbol{\phi}_l$, l =1,2, ..., L, derived from the EGF waveform G by

$$\phi_l(t) = G(t - l.\delta t), \tag{5}$$

i.e. the same Green's functions time-shifted to represent all the possible occurrence times of the aftershock. Here, $L = 2048$ is the number of samples of $\mathbf{u}$ and $\delta t = 0.01$ s is the sampling time interval. We build a matrix $\boldsymbol{\Phi}$ with columns formed by the basis functions $\phi_1, \ldots, \phi_L$. The target waveform is related to the RSTF $\mathbf{s} \in \mathbb{R}^L$ by

$$\mathbf{u} = \boldsymbol{\Phi}\mathbf{s}. \tag{6}$$

We hypothesize that the signal can be reconstructed by a small number m of basis functions, $m \ll L$, that is, the RSTF has a maximum of m non-zero values. We express our deconvolution problem as

$$\text{minimize} \qquad ||\mathbf{r}||_2 = ||\boldsymbol{\Phi}\mathbf{s} - \mathbf{u}||_2, \tag{7}$$

$$\text{subject to:} \qquad \text{Card}\{\mathbf{s} \neq 0\} \leq m, \tag{8}$$

$$\mathbf{s} > 0. \tag{9}$$

The two constraints enforce sparsity and positivity, respectively. We solve the problem in Eqs. (7-9) by the Orthogonal Matching-Pursuit algorithm [*Tropp and Gilbert*, 2007]. The approach is similar to that of *Kikuchi and Kanamori* [1991]. We start from an initial null guess $\mathbf{s} = 0$, residual $\mathbf{r_0} = \mathbf{u}$ and set the iteration counter to $h = 1$. We then identify the basis function that best matches the current residual,

$$n_l = \arg\, \max_{l=1,L} \boldsymbol{\phi}_l^{\mathrm{T}}\, \mathbf{r_{h-1}}. \tag{10}$$

We add the identified basis function to the set already obtained at the previous iterations, $\mathbf{\Gamma}_t = \mathbf{\Gamma}_{h-1} \cup n_l$, $(\mathbf{\Gamma}_0 = \emptyset)$. We then solve a positive least squares problem, minimizing

$$||\mathbf{\Phi}(\mathbf{\Gamma_h})\mathbf{s} - \mathbf{u}||_2, \tag{11}$$

under positivity constraint, $\mathbf{s} > 0$. This yields a new estimate of the RSTF, $\mathbf{s}_h$, and the updated residual $\mathbf{r}_h = \mathbf{u}_h - \mathbf{\Phi}(\mathbf{\Gamma_h})\mathbf{s}_h$ (Figure 6). We finally repeat the iteration procedure until $h = m$ or until convergence (no significant update) is reached. Here we set $m = 10$. Like for the Landweber deconvolution technique, we stack the RSTF obtained at different stations to obtain the STF of each event.

For most of the 64 analyzed events, the sparse deconvolution technique validates the STF obtained previously, i.e. it yields a very similar, but obviously more sparse STF (Figure 6). Ten STFs obtained by sparse deconvolution do not present any clear peak, and also correspond to weak peaks in the STF obtained by Landweber deconvolution. The remaining 54 STFs show a clear secondary peak in both deconvolution methods and constitute our final set of early aftershocks. We finally extract from the identified peaks, the occurrence time Δt of the aftershocks relative to their mainshock.

4. Aftershock Locations and Magnitudes

4.1. Computing Time Delays

We are interested in locating the detected aftershocks relative to their mainshock. We already have some information. First, the high similarity between mainshock and aftershock waveforms suggests that the two events are very close to each other. Furthermore, the emergence of a peak in the STF by stacking the RSTFs of individual stations is only possible if the two events are close. The peaks in the STFs are clear and their width does not exceed 0.03 s (3 samples). To locate the aftershocks we first recover their waveforms. This is a difficult task as aftershock signals are strongly contaminated by the mainshock coda. We set the first 10 samples (0.1 s) of the RSTF to zero, then convolve it with the EGF. This effectively removes the contribution of the mainshock. This technique performs better than a simple subtraction of the scaled EGF waveform. We then isolate a 2.56 long window around the P-wave arrival of the aftershock and mainshock waveforms. At each station, we determine the arrival time difference between mainshock and aftershock as the time lag that maximizes the correlation function of their waveforms. The search is restricted to time lags within 0.05 s of the relative interval Δt of the stacked STF. Sub-sample precision differential times, dt, are estimated by quadratic interpolation of the correlation function. For each mainshock-aftershock pair we finally obtain a set of differential arrival times dt at each station, computed from all available EGFs.

4.2. Aftershock Relative Locations

Relative locations are here obtained by a cascaded Metropolis algorithm [*Mosegaard and Tarantola*, 2002]. We perform a random walk, that samples the posterior probability density distributions of the model parameters $\rho(\mathbf{m})$, where $\mathbf{m} = \{\delta x, \delta y, \delta z, \delta t_0\}$ is the vector containing the model parameters, i.e. the relative 3D position and origin time between mainshock and aftershock. The data are given by the computed time delays, $\mathbf{d} = dt$. The initial guess is $\delta x = 0$, $\delta y = 0$, $\delta z = 0$, $\delta t_0 = \langle dt \rangle$, i.e. co-located with the mainshock. We then draw a set of random parameters around the initial guess. The new parameters are drawn from a Gaussian distribution centered on the parameters estimated at the previous step and with a standard deviation of 100 m for relative distances and 0.1 s for relative times. Given this new set of parameters we compute the expected time delays, dt_{calc},

$$dt_{calc}(\mathbf{m}) = \frac{1}{c_p} \left[\delta x \sin(\theta) \sin(\phi) + \delta y \cos(\theta) \sin(\phi) + \delta z \cos(\phi) \right] + \delta t_0; \tag{12}$$

where θ is the azimuth between the earthquake and the station, ϕ is the take off angle and c_p is the P-wave velocity in the source area. The negative log-likelihood, $l(\mathbf{m})$ for this new set of parameters is obtained as

$$l(\mathbf{m}) = \frac{|dt_{calc} - dt|}{\sigma_{dt}} \tag{13}$$

where σ_{dt} is the uncertainty associated to a measurement of dt and is based on the correlation coefficient of the measured time delays. We adopt the L_1 norm to reduce the influence of outliers during the inversion procedure. The new set of parameters is accepted as a sample of the distribution ρ if $l(\mathbf{m}) < l_0$ or if $\ln(X) < (l_0 - l(\mathbf{m}))$ with X a random number taken from a uniform distribution in [0–1] and l_0 the negative log-likelihood of the latest obtained sample of ρ. We then iterate the process and repeatedly draw another set of random parameters until we have at least 1000 samples of ρ.

We find that the mean horizontal distance between mainshocks and aftershocks is 56 m. Out of the 54 events, 51 have a horizontal separation shorter than 100 m. The remaining three events also have the least well resolved relative locations, with the highest uncertainties. For a robust analysis of the event locations we only keep those events for which the location uncertainties in both δx and δy (measured as the standard deviation of the distributions) are smaller than 20 m (Figure 7). This selected subset consists of 38 events out of the initial 54. The aftershocks that have poorer location accuracy are mostly associated with the lowest peaks in the STF, corresponding to aftershocks of relatively small magnitude compared to their mainshock. The relative locations of the majority of the well-located aftershocks appear to be in agreement with the inferred mean orientation of the San-Andreas fault near Parkfield, N150E [*Thurber et al.*, 2006] (Figure 7). All selected aftershocks occur close to their mainshock, confirming that the identified peaks in the STF are truly associated to aftershocks. We estimated mainshock rupture dimensions from catalog magnitude converted to moment using the relation of *Bakun* [1984] and assuming a circular rupture with constant stress drop of 1 MPa. The well-located aftershocks are located within 1 to 2 rupture lengths of their mainshock, but it is difficult to assess if they occur within the mainshock rupture area or at its edge as observed by *Rubin and Gillard* [2000].

We also observe an asymmetry of aftershock locations, with 26 out of 38 (2/3) aftershocks occurring to the NW of their mainshock. We quantify the significance of the observed asymmetry by testing against the null hypothesis that the aftershock relative locations result from a Bernoulli trial with two outcomes of equal probability: NW or SE location. Under the null hypothesis, the probability, P, of observing at least 26 out of 38 events in a preferred direction is given by

$$P = 2 \sum_{k=26}^{38} \binom{n}{k} p^k q^{n-k} \tag{14}$$

where $p = q = 0.5$ and $n = 38$. This gives P = 3.5 %. It is thus quite unlikely that the observed asymmetry is the result of random drawing from an equal outcome binomial distribution. This supports the observed asymmetry as a real feature of the early aftershock seismicity.

4.3. Aftershock Magnitudes

We estimate the magnitude of the newly detected aftershocks. We proceed by computing the amplitude of the aftershock peak in the STF relative to the mainshock peak, A_{AM}. To account for the width of STF peaks, we define A_{AM} based on the sum the STF amplitude over 3 time samples (0.03 s) around a peak. The relative STF amplitudes are equivalent to a relative moment. We convert them to a magnitude difference following *Bakun* [1984]'s relation for earthquakes in Central California. The aftershock magnitude M_A is

$$M_A = M_M + \frac{1}{1.2}\log_{10}(A_{AM}) \tag{15}$$

where M_M is the mainshock magnitude. We repeat the operation at all stations and for all possible EGFs, then average to obtain our final estimate of M_A for each aftershock. We obtain an average value of $\langle M_A \rangle = 1.05$ for all 54 identified aftershocks. In comparison, the mean magnitude for the 2414 events in the RES catalog is 1.52. Hence our method detects events of lower magnitude than in the original catalog.

5. Temporal Distribution of Sub-Events

We analyze the temporal organization of the detected early aftershocks and compare it to that of later aftershocks listed in the original catalog ($>$ 20 s). This comparison accounts for differences in detection threshold between the two catalogs. On the one hand, early aftershocks are more difficult to detect due to interference by the mainshock coda.

On the other hand, our method detects smaller earthquakes than in the original catalog. To account for changes of detection capability across time scales we first compute the magnitude distribution of events listed in the original catalog. We observe that the magnitude distribution is well fitted by a model that combines a probability function of detecting earthquakes and the Gutenberg-Richter distribution [*Ogata and Katsura*, 1993]. The best fit to this model gives $b = 1.0$ for the Gutenberg Richter law. The estimated magnitude of completeness is $m_c = 1.2$ (Figure 8). We assume that the magnitude distribution of the 54 newly detected events can be described by a similar model with $b = 1.0$ but with a different value of m_c. Due to the low number of events for this new population of events, we impose the value of b to reduce the uncertainty on the estimation of m_c. We found by fitting the distribution to the model of *Ogata and Katsura* [1993] that $m_c = 0.8$. The difference of the magnitude of completeness of the two catalogs is $\Delta m_c = 1.2 - 0.8 = 0.4$. In order to compare the rates of aftershocks in the two catalogs, we correct the aftershock rate derived from the original catalog by the factor $\alpha = 10^{\Delta m_c} = 2.5$. We then build a composite aftershock sequence. We treat each event in the repeating earthquake catalog as a potential mainshock and all subsequent events of the same sequence as aftershocks. Based on the time delay between events in a given sequence we then compute the rate of earthquakes following a each mainshock. We then stack results obtained for all sequences to obtain a composite aftershock sequence. In a second step we add to the already existing repeating sequences the new events detected with our deconvolution technique. We only consider earthquakes occurring before the 2004 Parkfield $\mathrm{M_w}6$ earthquake, to avoid the influence of the major stress perturbations it caused. This selection reduces the number of new events to 44. The aftershock rate computed from catalog data is multiplied by the factor α to account for the difference of completeness of the two catalogs. The resulting evolutions of aftershock rate are shown in figure 9. The early aftershock rate implied by the new events we detected agrees with the extrapolation to early times of the Omori-type behavior deduced from the original catalog. Notably, we resolve the emergence of the power-law decay starting at ~ 0.3 s after the mainshocks, that is, a time scale one order-of-magnitude longer that the mainshock rupture durations. The earthquake rate several years after a repeating earthquake deviates from Omori's law because repeating micro-earthquakes at Parkfield occur quasi-periodically with a recurrence time of about a year.

We tested, through synthetic tests, if the detection threshold of our method depends on the time since mainshock and on the mainshock magnitude. The tests are presented in Appendix B. We find that the detection threshold does not vary with time since mainshock. We also find that the changes of detectability related to the mainshock magnitude are not very large and when taken into account give similar results as the one presented in figure 9.

6. Discussion

Our detection method recovers early aftershocks of micro-earthquakes ($M_L = 0.9$ to 3.2), previously missed because hidden in the mainshock signals, down to ~ 0.3 s after the mainshock initiation. Our method is currently limited at short time-scales by noise and frequency content of the waveform data. The resolvable mainshock-aftershock time separation is limited by the width of the source time functions retrieved by deconvolution, which depends on noise level and dominant waveform period, in turn controlled by attenuation or rupture duration and filter high-frequency cutoff.

Most previous studies of early aftershock rates focused on a single aftershock sequence, notably following large magnitude events. To compare our study with these others studies, we normalize the earliest resolvable time of the aftershock rate by the mainshock rupture duration. Considering a typical dimension of 100 m for the events considered in our study and a rupture speed of 3 km/s, the typical rupture duration is 33 ms. This is 10 times shorter than the time scale of emergence of power-law decay found here, $\sim 0.3s$. This factor of 10 separation is similar, for example, to the one resolved for the 2004 M_w6 Parkfield earthquake: *Peng et al.* [2006] resolved aftershock rates starting 130 s after the mainshock onset and the estimated mainshock rupture duration is $\sim$ 6 s *Fletcher et al.* [2006]. Despite this similarity of relative time scales, most studies of early aftershocks of large events infer a departure from Omori's power-law decay at early times, i.e. a slower decay rate just after the mainshock than predicted by extrapolating the later Omori-type decay [e.g. *Peng et al.*, 2006]. In contrast, our results show that the aftershock rate shortly after the end of the mainshock rupture decays according to Omori's power-law, i.e. no flattening is observed down to the lowest resolvable time scale (figure 9). Multiple explanations of such a difference can be proposed: i) repeating earthquake sequences, which are the specific focus of our study, might have different aftershock sequences than the rest of the seismicity; ii) aftershock sequences may behave differently for large and small magnitude mainshocks; iii) the magnitude correction applied in large-mainshock studies is different from the one used in this study because of the severe effect of mainshock coda, and may result in underestimation of the early aftershock rates in previous studies. The constant aftershock decay exponent we resolve over the entire time span suggests that micro-earthquake triggering results from the same physical processes from scales of

0.3 s up to 100 days. It is naturally conceivable that at even earlier times aftershock activity is controlled by different triggering processes related to dynamic stresses carried by mainshock waves. This is supported by the analysis of *Wang et al.* [2014] to resolve aftershocks occurring at times shorter than 0.2 s and located close to their mainshocks. They detected events at these short time scales through a parametric inversion procedure applied to sub-sampled waveforms.

The relative timing and location of these very early aftershocks are consistent with the passage of shear waves radiated by the mainshock.

Wang et al. [2014] detected overall 153 aftershocks within a distance of 2 mainshock rupture radii, out of a total of 20990 possible mainshocks. They also found that 100 out of these 153 events occurred near the mainshock S-wave front and their relative locations showed a pronounced asymmetry, favoring aftershock triggering to the SE of their mainshocks. This corresponds to the preferred rupture direction predicted by theory and simulation of dynamic rupture on bimaterial faults [*Rubin and Ampuero*, 2007; *Ampuero and Ben-Zion*, 2008], consistent with rupture directivity observations [*Wang and Rubin*, 2011], and the bimaterial structure in the Parkfield area [*McGuire and Ben-Zion*, 2005; *Lengliné and Got*, 2011; *Kane et al.*, 2013]. Here we found more aftershocks located in the opposite direction (NW). We investigate if this asymmetry changes with time since the mainshock. We compute the ratio between the number of NW events and the number of SE events that occurred since the mainshock time for various time intervals. We find that this asymmetry is largest at the earliest times in our study, from 0.3 s to about 1 min, and then decreases progressively (figure 9-bottom). Such aftershock asymmetry, opposite to the preferred rupture direction, has been previously observed over long time scales of 10 s to 9 hrs [*Rubin and Gillard*, 2000; *Rubin*, 2002], and up to two days [*Zaliapin and Ben-Zion*, 2011]. The earthquakes resolved here hence belong to this population of longer-term aftershocks, rather than to the very early events triggered dynamically. *Wang et al.* [2014] proposed that the excess of aftershocks to the SE at very early times could account for the events missing in the SE in the longer term (10 s– 9 hours) aftershock population, if sites are allowed to break only once during the whole aftershock sequence. Our results imply that the shift of the direction of aftershock asymmetry occurs less than 0.3 s after the mainshock. Aftershocks in the preferred rupture direction on bimaterial faults (here, SE) were proposed to result from a tensile stress pulse propagating with the rupture front of the mainshock in the preferred rupture direction [*Rubin and Ampuero*, 2007; *Wang et al.*, 2014]. Aftershocks at longer time scales (here, 0.3 s 100 days) result from a different mechanism.

The early aftershocks identified in our study may result from static stress transfer directly from the mainshock rupture or indirectly from its afterslip. Afterslip can reproduce the $1/t$ aftershock rate decay, and is constrained by our results to start earlier than 10 times the mainshock rupture duration [*Helmstetter and Shaw*, 2009]. Aftershock migration is predicted by models where aftershocks are driven by an expanding afterslip front [e.g. *Kato*, 2007]. The persistence of aftershock asymmetry on bimaterial faults up to long times remains unexplained by current numerical models [*Rubin and Ampuero*, 2007], but the possibility of asymmetric afterslip has not been explored. While we do not observe aftershock migration in our results, resolving it would require the detection of more distant aftershocks, but this is limited by our selection criteria and our focus on similar events. Thus we cannot rule out the afterslip-driven model on the basis of lack of observed aftershock migration. The asymmetric residual stresses left by the mainshock rupture on a bimaterial fault *Rubin and Ampuero* [2007] could contribute to asymmetry of afterslip, even without migration.

In the context of rate-and-state friction models of aftershocks triggered by coseismic static stress steps, the onset time c of power-law aftershock rate decay is related to frictional parameters [*Dieterich*, 1994] by

$$c = t_a \exp\left(\frac{-\Delta\tau}{a\sigma}\right), \tag{16}$$

where t_a is the aftershock duration, in the range 0.5 to 5 years in this region [*Toda and Stein*, 2002], $\Delta\tau$ is the average shear stress change caused by the mainshock rupture, a is a rate-and-state friction parameter quantifying the importance of the immediate logarithmic velocity-strengthening effect, and σ is the effective normal stress. Considering $c < 0.3$ s and the lower bound $t_a = 0.5$ years, we estimate $\Delta\tau/a\sigma > 20$. This lower bound on the stress stimulus is consistent with the idea that the stress transferred to the immediate vicinity of a rupture is higher than the stress drop within the rupture, which scales in the rate-and-state friction model as $(b-a)/\sigma \log(V_{dyn}/V_{load}) \sim 20(b-a)\sigma$ [e.g. *Perfettini and Ampuero*, 2008]. Most of the aftershocks we resolve are located near the edge of their mainshock rupture but we acknowledge important relative location uncertainties, notably because we estimate mainshock sizes assuming a constant stress drop for all events. High stress concentrations triggering aftershocks within the nominal mainshock rupture area are also possible if its slip distribution is heterogeneous [e.g. *Herrero and Bernard*, 1994; *Mai and Beroza*, 2002]. Considering the regional upper bound of earthquake duration, $t_a = 5$ years, would lead to even larger estimates of stress transfer. Coseismic stresses that high are not expected to prevail over distances larger than one mainshock radius, but may be accounted by stress transfer via afterslip.

7. Conclusion

By analysing precisely early aftershocks of similar micro-earthquakes in Parkfield, California, we extend the resolution of aftershock rates down to 0.3 s after the mainshock origin time, that is, ~ 10 times the mainshock rupture duration. Over a time scale span of nearly 8 orders of magnitude, from 0.3 s up to more than 100 days, the aftershock rate decay is well described by a single Omori power-law with no flattening at early times. If a characteristic time for the onset of the power-law regime exists, it is necessarily shorter than 0.3 s. Our results suggest that aftershocks occurring beyond the time scales of dynamic triggering arise from relatively large stress perturbations, possibly caused by aseismic afterslip with very short characteristic time. We also observe an asymmetry of aftershock relative locations along-strike, persistent over long periods and consistent with previous observations on bimaterial faults.

Appendix A: Comparison with the Template-Matching Approach

We consider the example shown in Figure 4. We compute the cross-correlation function between the signal with sub-event and the signal without sub-event (from another earthquake of the same repeating sequence). We also compute for reference the auto-correlation function of both signals. A second peak of the correlation function appears at the time of the sub-event (Figure 10) and is about twice as high as other nearby secondary peaks. In contrast, the peak associated with the sub-event in the RSTF obtained by Landweber deconvolution (also shown in Figure 10) is about one order of magnitude higher than all other RSTF peaks. This example illustrates that, when the aftershock signal is dominated by the mainshock signal, the template matching approach has a poorer sub-event detection capability than our deconvolution method.

Appendix B: Synthetic Tests on Detection Thresholds

We perform synthetic tests to estimate the detection capability of our deconvolution method. We select randomly 50 events in the repeating earthquakes catalog. We ensure that none of these events contains a sub-event in the first 20 s. We add a duplicate of the mainshock signals with various time delays and amplitudes relative to the mainshock. Relative time delays are set at 0.05, 0.1, 0.2, 0.3, 0.5, 1, 2, 3, 5, 10, and 15 s. Relative maximum amplitudes are set to 0.005, 0.01, 0.03, 0.1, 0.3, and 0.5. We then run our deconvolution sub-event detection process. We first find that, for all events, the inter-event time has no influence on the detection capability as long as the sub-event occurs later than 0.2 s after the mainshock (see Figure 11).

The minimum relative amplitude of the sub-event that is detected varies with the mainshock magnitude. For a magnitude 1.2 event we can detect sub-events down to a relative amplitude of 0.1, which corresponds to a minimum magnitude of $1.2 - \frac{1}{1.2}\log_{10}(0.1) = 0.4$. For a larger mainshock (m=3.0) detection is possible down relative amplitude of 0.01, or a sub-event magnitude as low as $3.0 + \frac{1}{1.2}\log_{10}(0.01) = 1.3$. The minimum resolvable magnitude evolves between these two values as a function of mainshock magnitudes, although the scatter is important. We define the magnitude detection threshold for a mainshock of magnitude m based on a linear fit of the detection thresholds obtained for the magnitude 1.2 and 3.0 events. We then corrected our aftershock rate, for the newly detected events, taking into account this change of detection threshold. We give a weight to each detected earthquake that depends on its probability of being detected (based on the mainshock magnitude). This results in the new aftershock rate shown in Figure 12. We note that this correction leaves unchanged the observation of a continuous decay of the aftershock rate over the whole considered period.

Acknowledgments. Data used in this study are from the Northern California Seismic Network, U.S. Geological Survey, Menlo Park (http://www.ncedc.org/ncsn/). We thank A. Rubin for numerous comments and Z. Duputel for discussion on the Metropolis Algorithm. We thank the associate editor and reviewers Y. Kagan and B. Enescu for suggestions. We acknowledge funding from NSF (grant EAR-1015698).

References

Ampuero, J.-P., and Y. Ben-Zion (2008), Cracks, pulses and macroscopic asymmetry of dynamic rupture on a bimaterial interface with velocity-weakening friction, *Geophys. J. Int.*, *173*(2), 674–692.

Bakun, W. H. (1984), Seismic moments, local magnitudes, and coda-duration magnitudes for earthquakes in central california, *B. Seismol. Soc. Am.*, *74*(2), 439–458.

Bertero, M., D. Bindi, P. Boccacci, M. Cattaneo, C. Eva, and V. Lanza (1997), Application of the projected Landweber method to the estimation of the source time function in seismology, *Inverse Problems*, *13*, 465–486, doi:10.1088/0266-5611/13/2/017.

Bosl, W., and A. Nur (2002), Aftershocks and pore fluid diffusion following the 1992 Landers earthquake, *J. Geophys. Res.*, *107*(B12), ESE–17.

Dieterich, J. (1994), A constitutive law for rate of earthquake production and its application to earthquake clustering, *J. Geophys. Res.*, *99*, 2601–2618, doi:10.1029/93JB02581.

Enescu, B., J. Mori, and M. Miyazawa (2007), Quantifying early aftershock activity of the 2004 mid-Niigata Prefecture earthquake (Mw6. 6), *J. Geophys. Res.*, *112*(B4).

Enescu, B., J. Mori, M. Miyazawa, and Y. Kano (2009), Omori-Utsu law c-values associated with recent moderate earthquakes in Japan, *B. Seismol. Soc. Am.*, *99*(2A), 884–891.

Fischer, T. (2005), Modelling of multiple events using empirical greens functions: method, application to swarm earthquakes and implications for their rupture propagation, *Geophys. J. Int.*, *163*(3), 991–1005.

Fletcher, J. B., P. Spudich, and L. M. Baker (2006), Rupture propagation of the 2004 Parkfield, California, earthquake from observations at the UPSAR, *B. Seismol. Soc. Am.*, *96*(4B), S129–S142.

Helmstetter, A., and B. E. Shaw (2009), Afterslip and aftershocks in the rate-and-state friction law, *J. Geophys. Res.*, *114*(B1).

Helmstetter, A., Y. Y. Kagan, and D. D. Jackson (2006), Comparison of short-term and time-independent earthquake forecast models for southern california, *B. Seismol. Soc. Am.*, *96*(1), 90–106.

Herrero, A., and P. Bernard (1994), A kinematic self-similar rupture process for earthquakes, *B. Seismol. Soc. Am.*, *84*(4), 1216–1228.

Kagan, Y. Y. (2004), Short-term properties of earthquake catalogs and models of earthquake source, *B. Seismol. Soc. Am.*, *94*(4), 1207–1228.

Kagan, Y. Y., and H. Houston (2005), Relation between mainshock rupture process and omori's law for aftershock moment release rate, *Geophys. J. Int.*, *163*(3), 1039–1048.

Kane, D. L., P. M. Shearer, B. P. Goertz-Allmann, and F. L. Vernon (2013), Rupture directivity of small earthquakes at Parkfield, *J. Geophys. Res.*, *118*, 212–221, doi: 10.1029/2012JB009675.

Kato, N. (2007), Expansion of aftershock areas caused by propagating post-seismic sliding, *Geophys. J. Int.*, *168*(2), 797–808.

Kikuchi, M., and H. Kanamori (1991), Inversion of complex body wavesiii, *B. Seismol. Soc. Am.*, *81*(6), 2335–2350.

Lengliné, O., and J.-L. Got (2011), Rupture directivity of microearthquake sequences near Parkfield, California, *Geophys. Res. Let.*, *38*(8).

Lengliné, O., and D. Marsan (2009), Inferring the coseismic and postseismic stress changes caused by the 2004 $M_w = 6$ Parkfield earthquake from variations of recurrence times of microearthquakes, *J. Geophys. Res.*, *114*, B10303, doi:10.1029/2008JB006118.

Lengliné, O., B. Enescu, Z. Peng, and K. Shiomi (2012), Decay and expansion of the early aftershock activity following the 2011, Mw9. 0 Tohoku earthquake, *Geophys. Res. Let.*, *39*(18).

Mai, P. M., and G. C. Beroza (2002), A spatial random field model to characterize complexity in earthquake slip, *J. Geophys. Res.*, *107*(B11), 2308.

McGuire, J., and Y. Ben-Zion (2005), High-resolution imaging of the bear valley section of the san andreas fault at seismogenic depths with fault-zone head waves and relocated seismicity, *Geophys. J. Int.*, *163*(1), 152–164.

Mosegaard, K., and A. Tarantola (2002), *Probabilistic Approach to Inverse Problems*, 237-265 pp., Academic Press.

Narteau, C., S. Byrdina, P. Shebalin, and D. Schorlemmer (2009), Common dependence on stress for the two fundamental laws of statistical seismology, *Nature*, *462*, 642–645, doi:10.1038/nature08553.

Ogata, Y., and K. Katsura (1993), Analysis of temporal and spatial heterogeneity of magnitude frequency distribution inferred from earthquake catalogues, *Geophys. J. Int.*, *113*(3), 727–738.

Parsons, T. (2005), A hypothesis for delayed dynamic earthquake triggering, *Geophys. Res. Let.*, *32*(4), L04,302.

Peng, Z., and P. Zhao (2009), Migration of early aftershocks following the 2004 Parkfield earthquake, *Nature Geoscience*, *2*(12), 877–881.

Peng, Z., J. E. Vidale, and H. Houston (2006), Anomalous early aftershock decay rate of the 2004 Mw6. 0 Parkfield, California, earthquake, *Geophys. Res. Let.*, *33*(17).

Peng, Z., J. E. Vidale, M. Ishii, and A. Helmstetter (2007), Seismicity rate immediately before and after main shock rupture from high-frequency waveforms in Japan, *J. Geophys. Res.*, *112*(B3).

Perfettini, H., and J.-P. Ampuero (2008), Dynamics of a velocity strengthening fault region: Implications for slow earthquakes and postseismic slip, *J. Geophys. Res.*, *113*(B9).

Piana, M., and M. Bertero (1997), Projected Landweber method and preconditioning, *Inverse Problems*, *13*, 441–463, doi:10.1088/0266-5611/13/2/016.

Rodriguez, I. V., M. Sacchi, and Y. J. Gu (2012), Simultaneous recovery of origin time, hypocentre location and seismic moment tensor using sparse representation theory, *Geophys. J. Int.*, *188*, 1188–1202, doi:10.1111/j.1365-246X.2011.05323.x.

Rubin, A. M. (2002), Aftershocks of microearthquakes as probes of the mechanics of rupture, *J. Geophys. Res.*, *107*(B7), 2142.

Rubin, A. M., and J.-P. Ampuero (2007), Aftershock asymmetry on a bimaterial interface, *J. Geophys. Res.*, *112*(B5).

Rubin, A. M., and D. Gillard (2000), Aftershock asymmetry/rupture directivity among central San Andreas fault microearthquakes, *J. Geophys. Res.*, *105*, 19,095–19,109.

Sawazaki, K., and B. Enescu (2014), Imaging the high-frequency energy radiation process of a main shock and its early aftershock sequence: The case of the 2008 iwate-miyagi nairiku earthquake, japan, *J. Geophys. Res.*, *119*(6), 4729–4746.

Schaff, D. P., G. C. Beroza, and B. E. Shaw (1998), Postseismic response of repeating aftershocks, *Geophys. Res. Let.*, *25*(24), 4549–4552.

Shelly, D. R., Z. Peng, D. P. Hill, and C. Aiken (2011), Triggered creep as a possible mechanism for delayed dynamic triggering of tremor and earthquakes, *Nature Geoscience*, *4*(6), 384–388.

Thurber, C., H. Zhang, F. Waldhauser, J. Hardebeck, A. Michael, and D. Eberhart-Phillips (2006), Three-Dimensional Compressional Wavespeed Model, Earthquake Relocations, and Focal Mechanisms for the Parkfield, California, Region, *B. Seismol. Soc. Am.*, *96*(4B), S38–S49, doi:10.1785/0120050825.

Toda, S., and R. S. Stein (2002), Response of the San Andreas fault to the 1983 Coalinga-Nuñez earthquakes: An application of interaction-based probabilities for Parkfield, *J. Geophys. Res.*, *107*(B6), ESE–6.

Tropp, J., and A. Gilbert (2007), Signal recovery from random measurements via orthogonal matching pursuit, *Information Theory, IEEE Transactions on*, *53*(12), 4655 –4666, doi:10.1109/TIT.2007.909108.

Utsu, T., Y. Ogata, and R. S. Matsu'ura (1995), The centenary of the Omori formula for a decay law of aftershock activity, *J. Phys. Earth*, *43*, 1–33.

Vallée, M. (2004), Stabilizing the Empirical Green Function Analysis: Development of the Projected Landweber Method, *B. Seismol. Soc. Am.*, *94*, 394–409, doi:10.1785/0120030017.

Wang, E., and A. M. Rubin (2011), Rupture directivity of microearthquakes on the San Andreas Fault from spectral ratio inversion, *Geophys. J. Int.*, *186*(2), 852–866.

Wang, E., A. M. Rubin, and J.-P. Ampuero (2014), Compound earthquakes on a bimaterial interface and implications for rupture mechanics, *Geophys. J. Int.*, p. ggu047.

Zaliapin, I., and Y. Ben-Zion (2011), Asymmetric distribution of aftershocks on large faults in california, *Geophys. J. Int.*, *185*(3), 1288–1304.

Figure 1. Map of the area, seismic stations (triangles) and earthquake epicenters (black dots) considered in this study. The earthquakes are part of a catalog of repeating earthquake sequences. The black triangles indicate stations that recorded at least 1000 of the 2414 repeating events. The black line corresponds to the surface fault trace of the San Andreas fault. In the regional map on the upper right corner, the gray box indicates the location of the study area.

Figure 2. Top : Waveform correlation coefficient between a single event and a synthetic doublet as a function of inter-event time of the doublet. The black line represents the average correlation coefficient for synthetics based on a set of 100 randomly selected events. The color lines show the correlation coefficient for a selection of 10 events with different magnitude. Bottom : same as upper figure showing a zoom at short inter-event times.

Figure 3. Waveforms of a repeating earthquake sequence comprising 9 events, ordered chronologically from bottom to top. Each record is 20.48 s long. The 8th event contains a high-frequency seismic signal arriving around 15 s after the first P-wave arrival (gray rectangle). This second event is hardly noticeable because its arrival is embedded within the S-wave coda of the first event.

Figure 4. a: Target (red) and empirical Green's function (EGF, blue) waveforms. The EGF is another event of the same RES as the target event. The two waveforms are highly similar during the entire 20 s window. b: Relative source time function (RSTF, black) obtained by EGF deconvolution. Its first peak corresponds to the main event and a second, smaller peak less than 1 s later indicates the occurrence of an aftershock. The inset is a zoom of the RSTF at early times. c: Target waveform (red) and waveform obtained by convoluting the RSTF with the EGF (blue). The perfect match between these two waveforms attests to the high performance of our deconvolution procedure. d: Reconstructed waveforms of mainshock (red) and aftershock (black) obtained by convolving the EGF with the RSTF after setting to 0 the RSTF segment before and after 0.1 seconds, respectively. The mainshock waveform has been aligned with the aftershock waveform to highlight their similarity, which attests to the proximity of the two events.

Figure 5. Result of EGF deconvolution for an earthquake of a repeating sequence. Each row represents in gray scale the RSTF obtained by deconvolution with a given EGF event of the sequence and at a given station. The black curve shown at the bottom is the STF obtained by stacking all the RSTFs. The plot on the right is an expanded view of the first 2 s (interval indicated by a vertical dashed line on the left plot). A coherent increase of RSTF amplitudes indicates the occurrence of an aftershock less than 1 s after the mainshock.

Figure 6. Top: Target waveform (black) and EGF waveform (red). Differences appear at around 6 s. Middle: Basis functions, $\phi_l(t)$, derived from the EGF waveform with a range of time shifts l. The two basis functions shown in red are identified by the sparse deconvolution as the major components of the target waveform. Bottom: STF obtained by sparse deconvolution (red) and by Landweber deconvolution (black). A clear peak at 4.5 s indicates the occurrence of an aftershock.

Figure 7. Map view of the locations of aftershock centroids relative to their mainshock. Each color corresponds to a different mainshock-aftershock pair. Only aftershocks with horizontal uncertainty smaller than 20 m are shown. For each aftershock we show 1000 samples of the posterior distribution (dots) and the average over all samples (stars). The dashed line show the mean strike of the San-Andreas fault at Parkfield.

Figure 8. Magnitude distribution for all events included in the repeating earthquake catalog (blue circles), and for the 54 new events detected (red circles). The blue and red line represent a fit to the distribution as proposed by *Ogata and Katsura* [1993].

Figure 9. Top: Composite earthquake rate, $\lambda(t)$, computed as the number of earthquakes per day following any event in a RES, considering all possible sequences of the catalog, with (red) and without (blue) the newly detected early aftershocks. The gray area is the typical duration of the mainshock rupture. Earthquake rate uncertainties are estimated from the 95% confidence interval of a Poisson distribution. The plain line is a power law fit for $\Delta t < 100$ days. We obtain a power-law exponent $p = 1.0$. The dashed line represents the Omori-Utsu law fit to the original catalog data following Eq. (1), yielding $c = 45$ s. Bottom: temporal evolution of the ratio between the cumulative number of well-located aftershocks to the NW and to the SE of their mainshock. Asymmetry is significant at early times, with preferred aftershock triggering to the NW, and progressively decreases after ~ 1 min.

Figure 10. Red and blue curves represent the autocorrelation function of the signal with and without sub-event, respectively, as a function of time. The black curve (barely visible behind the red one) is the correlation between these two signals. For reference, the source time function obtained by Landweber deconvolution, shifted vertically to a baseline of -1 for clarity is in green.

Figure 11. Top : Examples of source time functions obtained after deconvolving an event where the original signal has been duplicated at several time delays Δt and whose relative amplitude is 0.05 times the mainshock amplitude. The delays are indicated in the upper right corner. The peak in the source time function marks the occurrence of the sub-event. Bottom : Probability of detecting a sub-event as a function of the time delays computed from the 50 tested events. The colors indicate the relative amplitude of the tested events.

Figure 12. Same as figure 9 but with rate corrections applied to the newly detected events instead of to the original catalog.

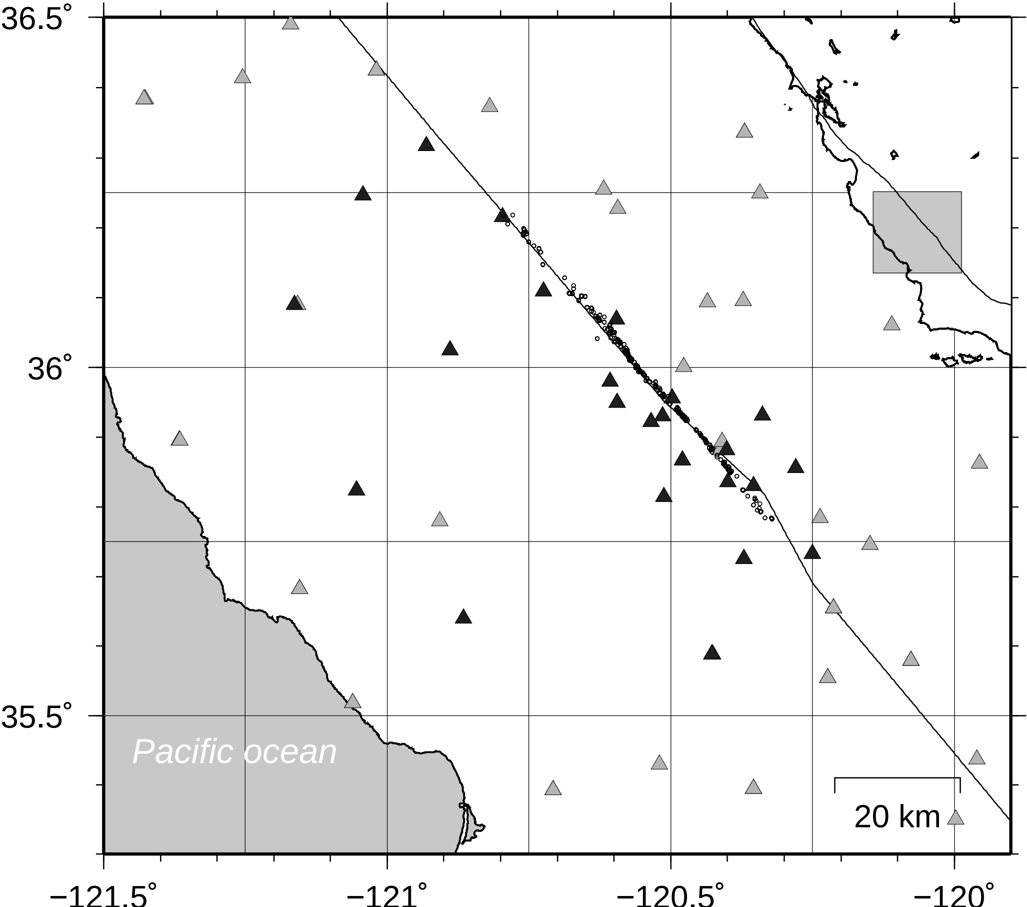
36.5°
36°
35.5°
−121.5°
−121°
−120.5°
−120°
Pacific ocean
20 km

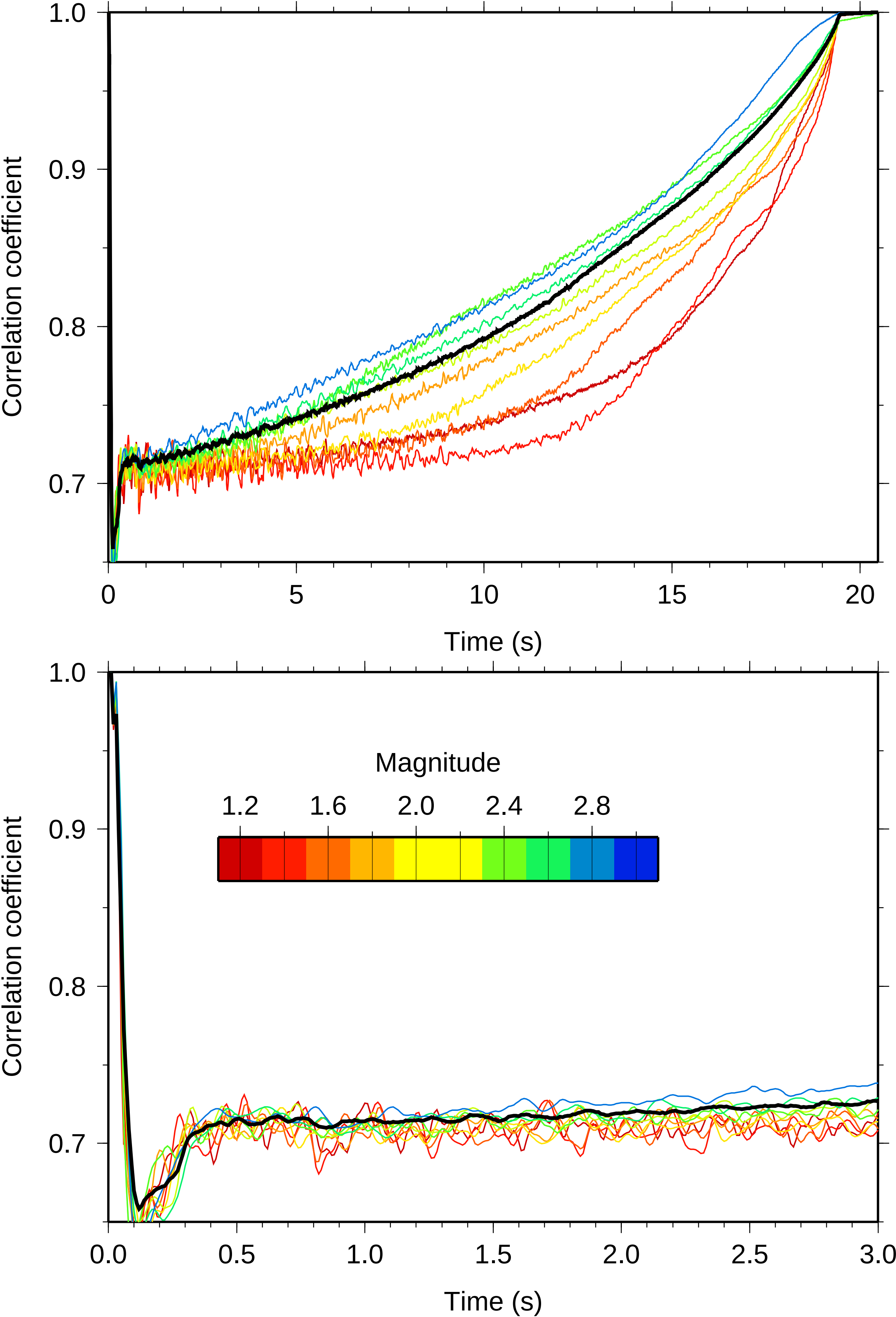
Correlation coefficient
1.0
0.9
0.8
0.7
0
5
10
15
20
Time (s)
Correlation coefficient
1.0
0.9
0.8
0.7
Magnitude
1.2
1.6
2.0
2.4
2.8
0.0
0.5
1.0
1.5
2.0
2.5
3.0
Time (s)

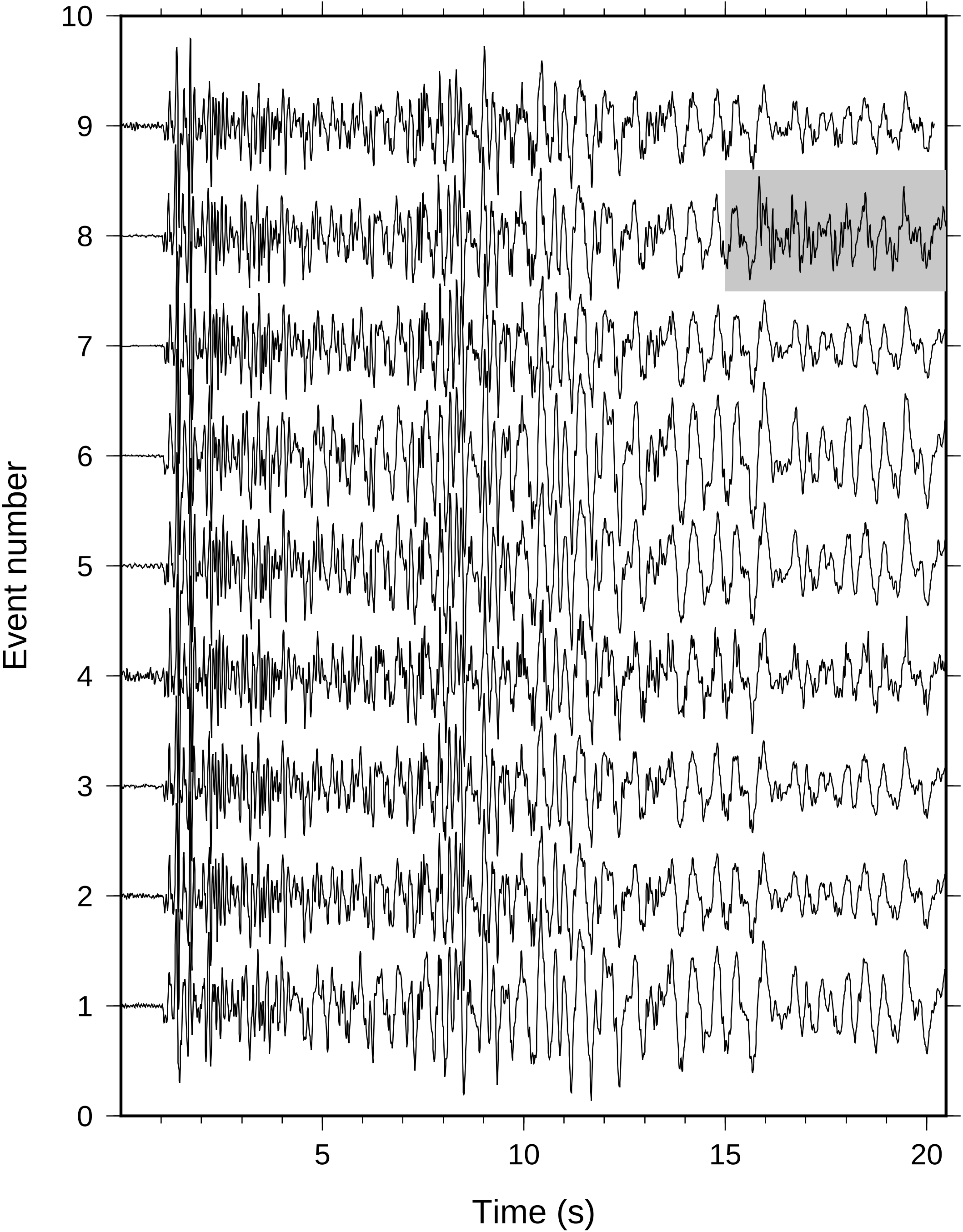
Event number
0
1
2
3
4
5
6
7
8
9
10
Time (s)
5
10
15
20

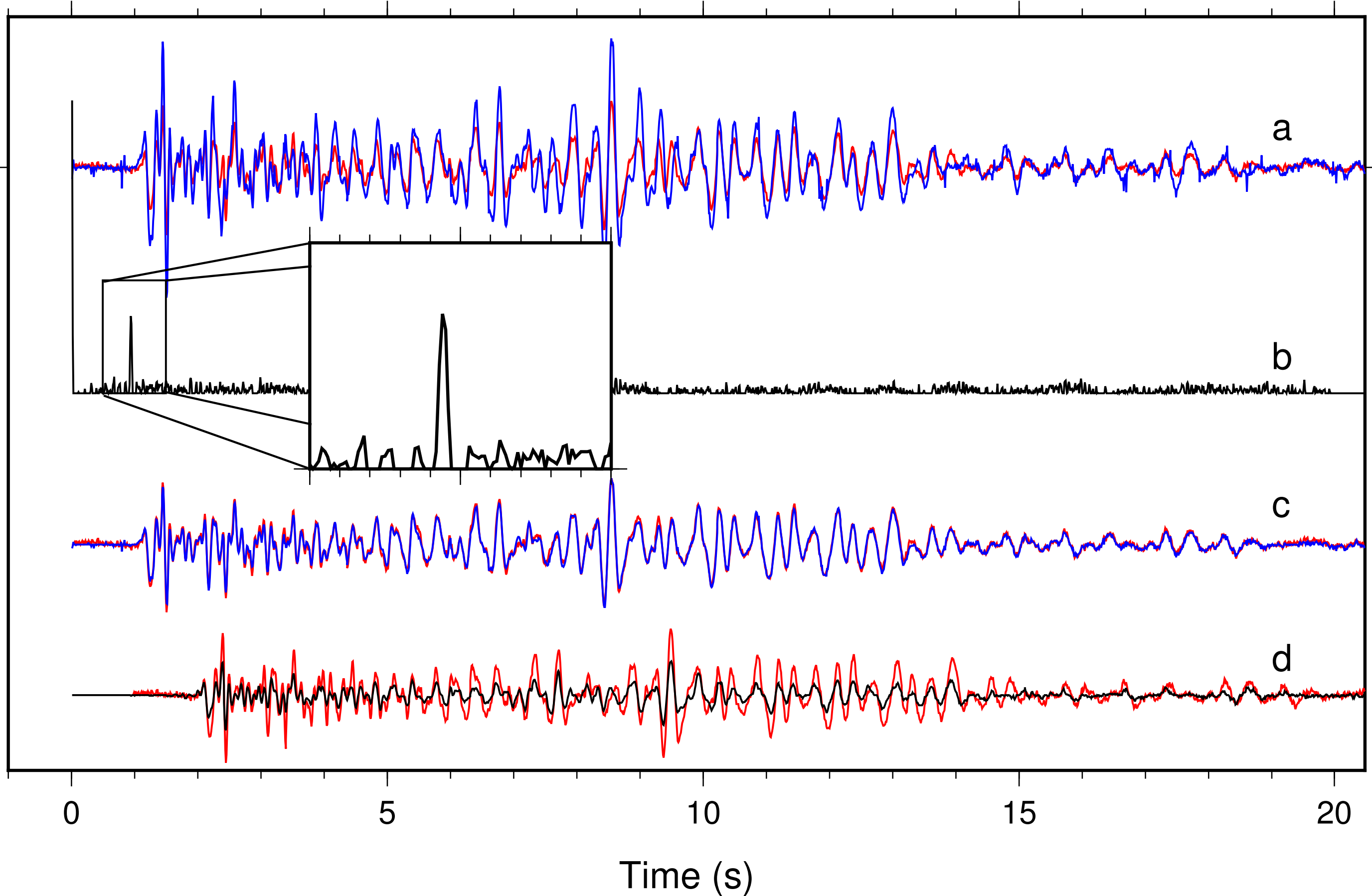
a
b
c
d
0
5
10
15
20
Time (s)

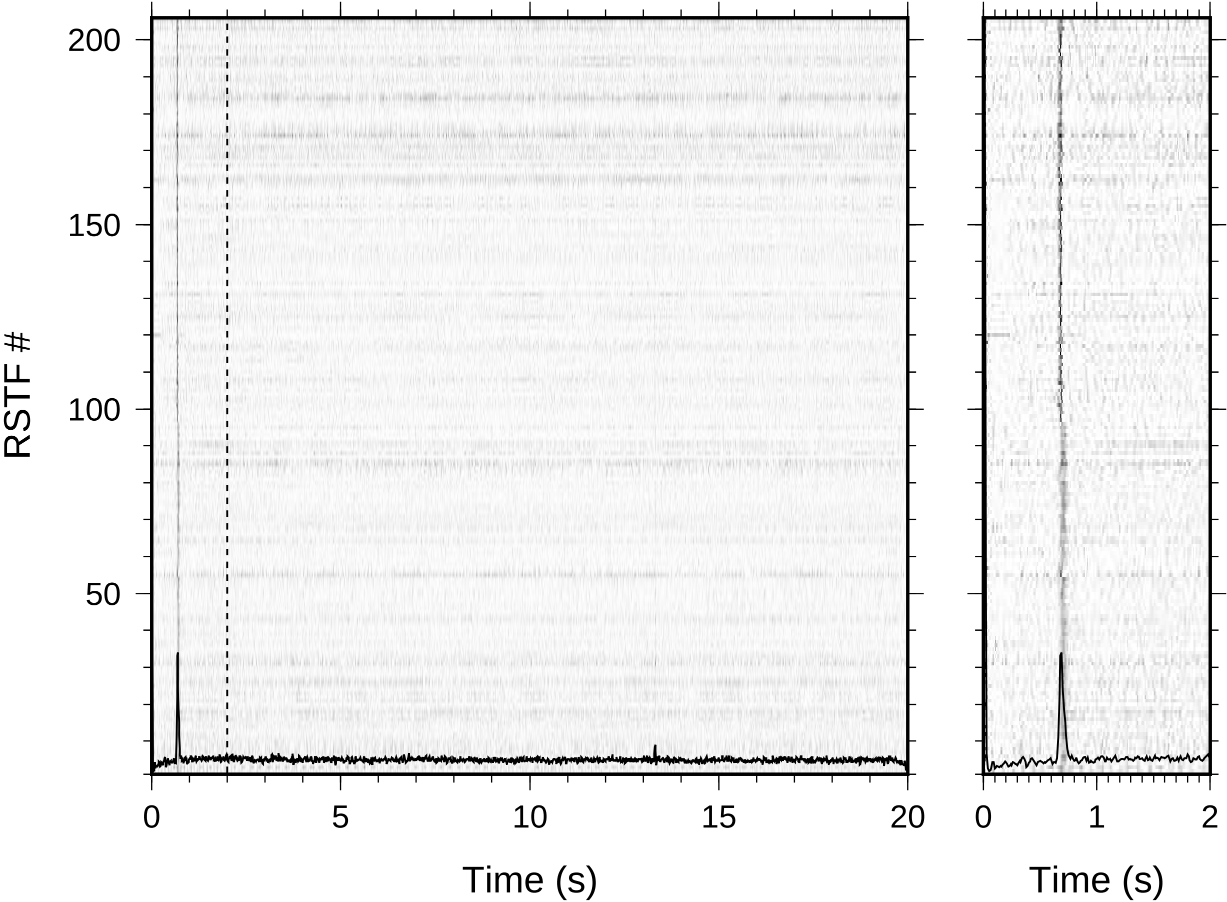
RSTF #
200
150
100
50
0
5
10
15
20
Time (s)
0
1
2
Time (s)

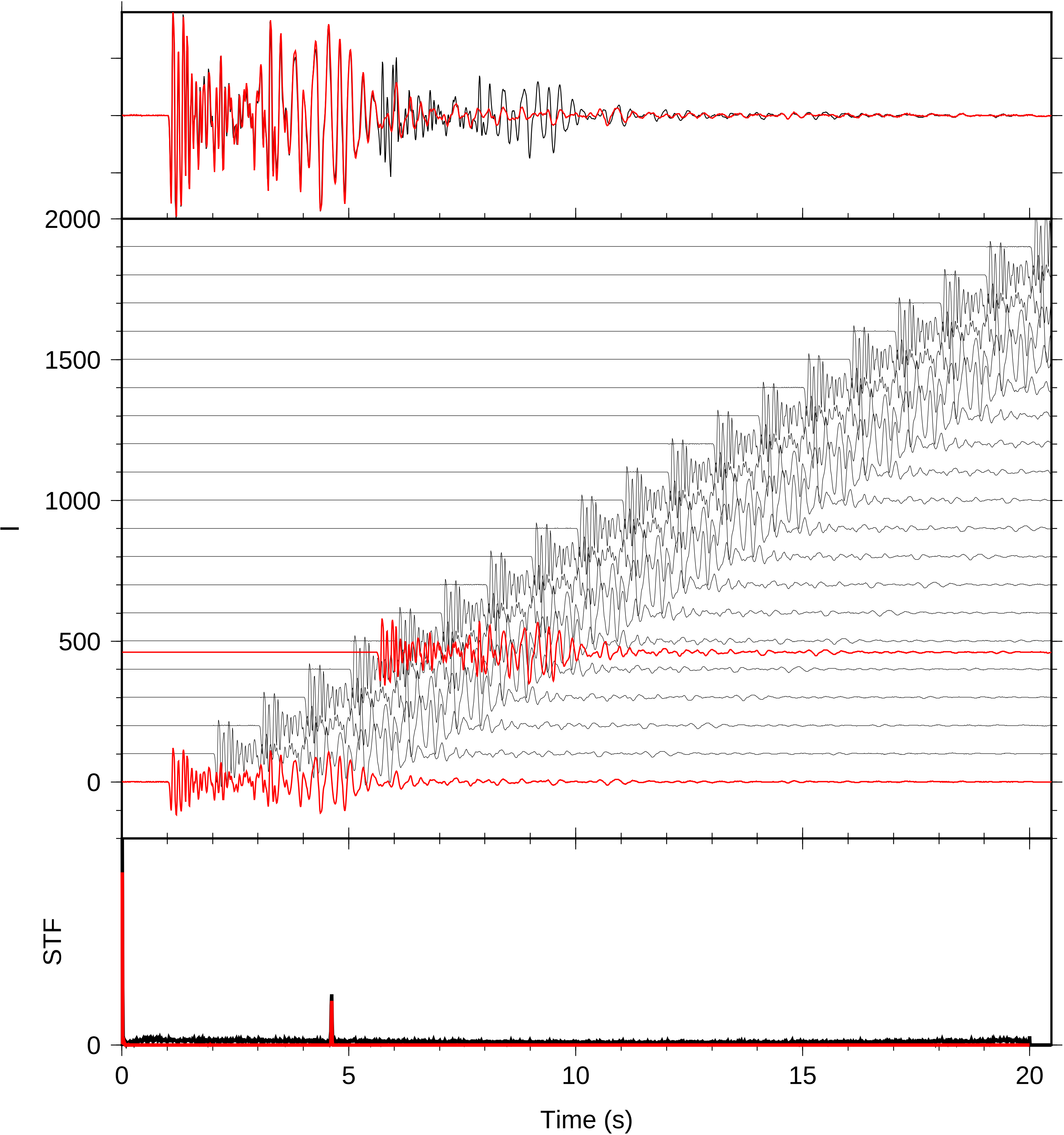
2000
1500
1000
500
0
I
STF
0
0
5
10
15
20
Time (s)

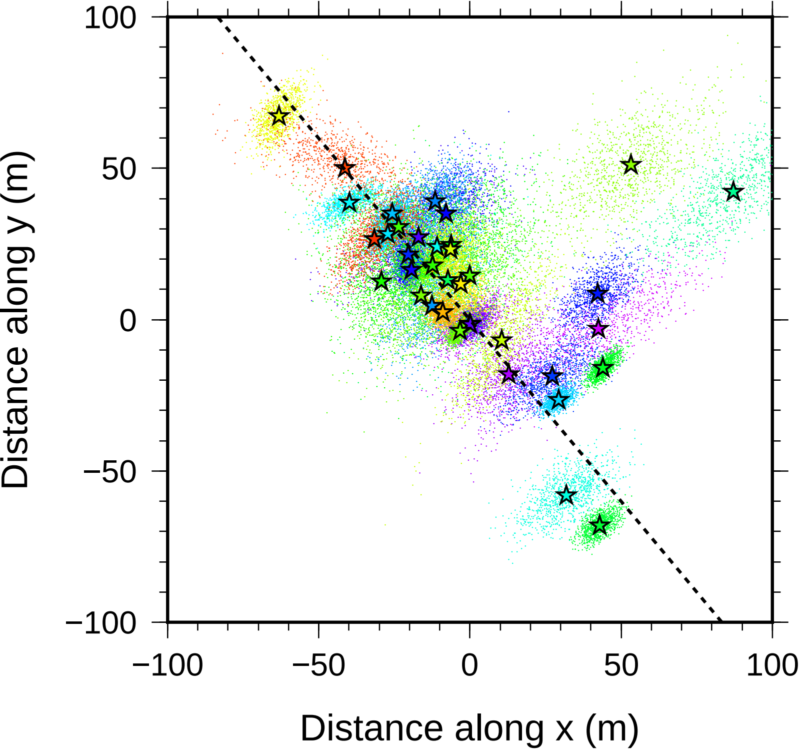
100
50
0
−50
−100
−100
−50
0
50
100
Distance along y (m)
Distance along x (m)

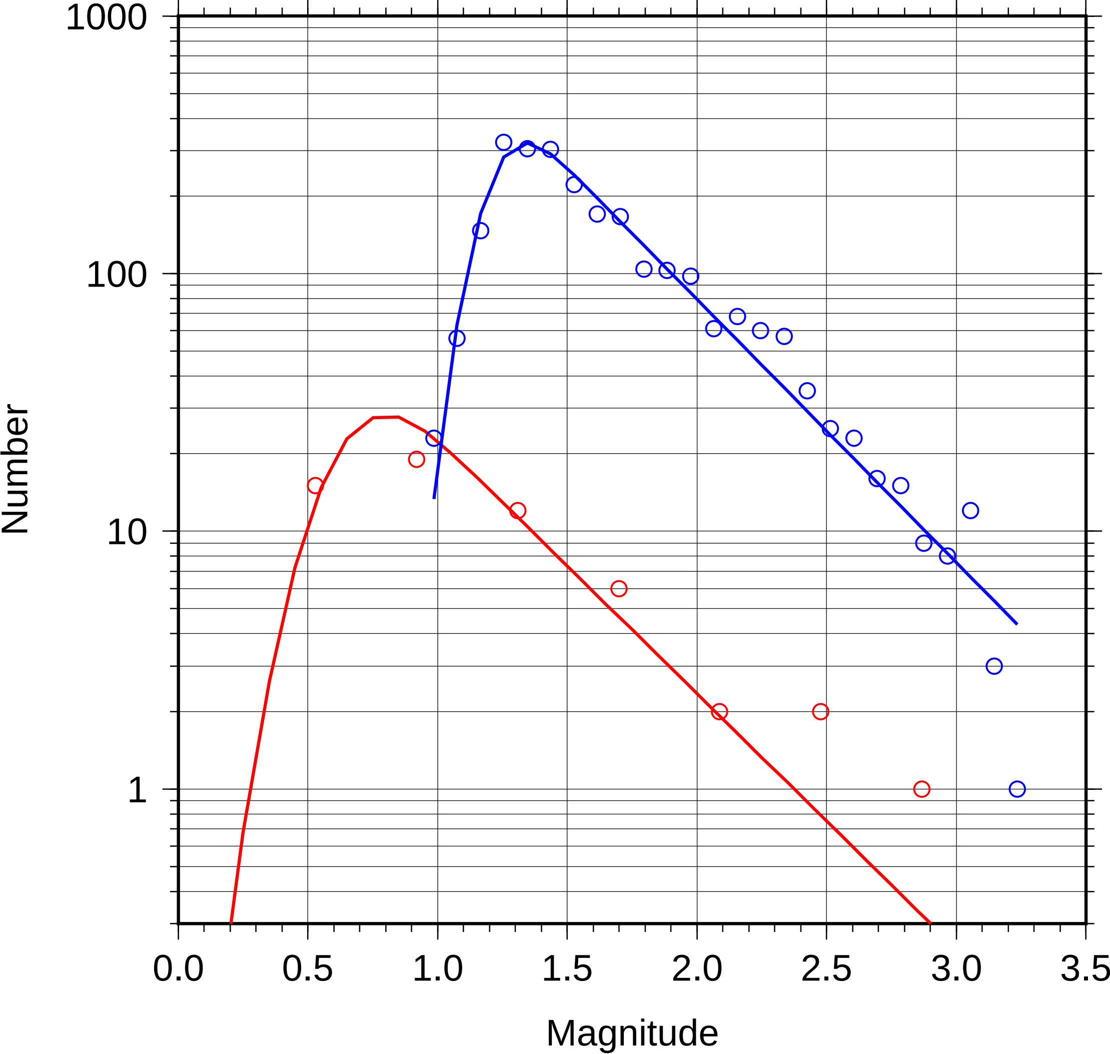
1000
100
10
1
Number
0.0
0.5
1.0
1.5
2.0
2.5
3.0
3.5
Magnitude

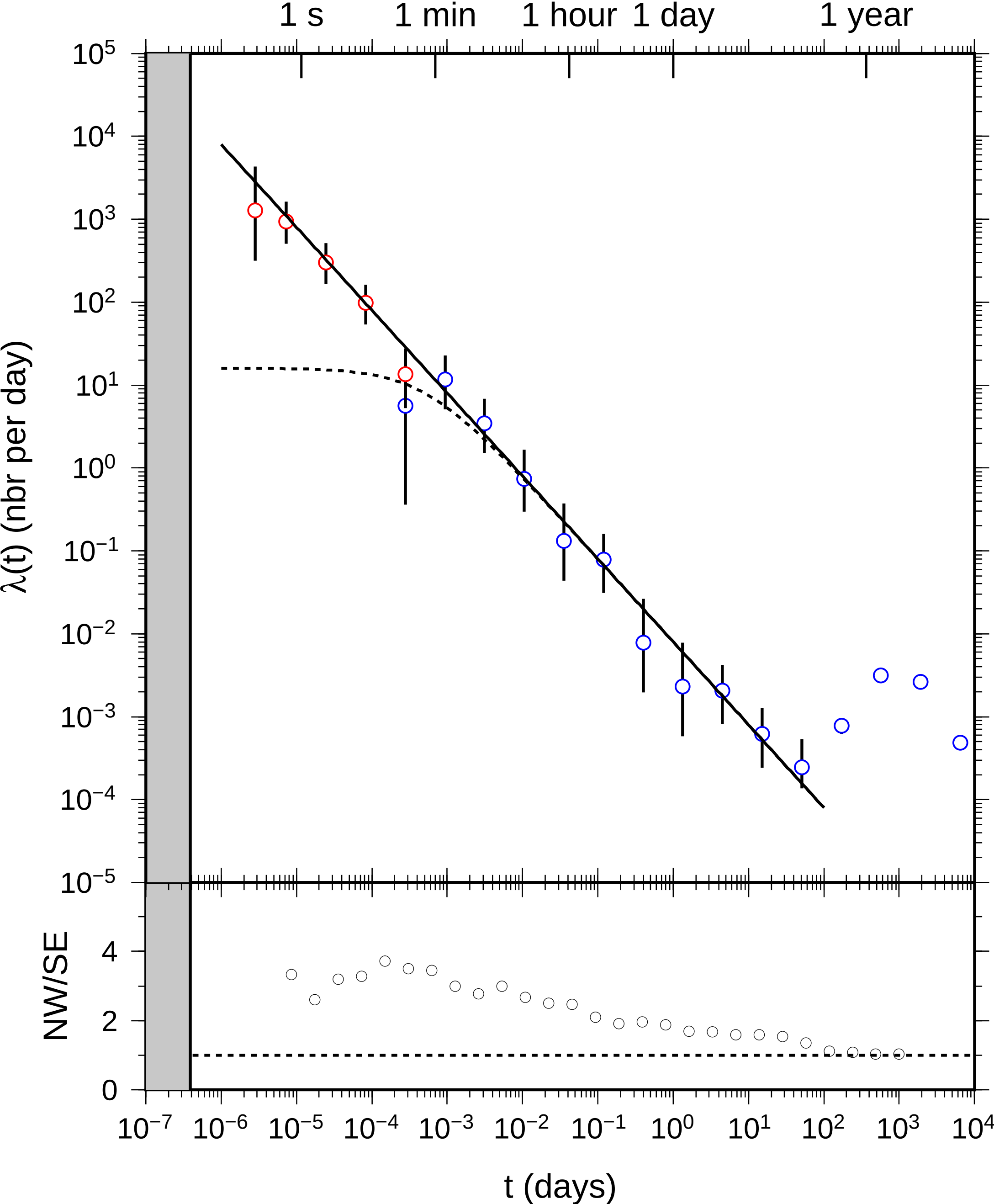
1 s
1 min
1 hour
1 day
1 year
10^5
10^4
10^3
10^2
10^1
10^0
10^{-1}
10^{-2}
10^{-3}
10^{-4}
10^{-5}
λ(t) (nbr per day)
NW/SE
4
2
0
10^{-7}
10^{-6}
10^{-5}
10^{-4}
10^{-3}
10^{-2}
10^{-1}
10^0
10^1
10^2
10^3
10^4
t (days)

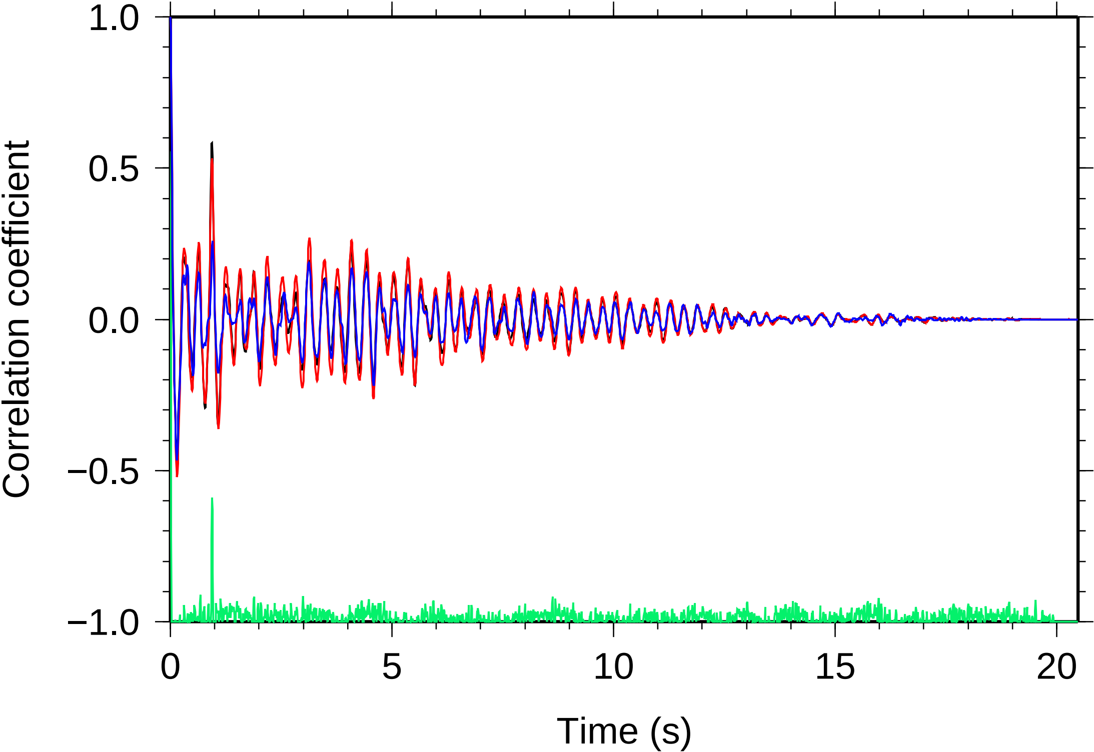
1.0
0.5
0.0
−0.5
−1.0
Correlation coefficient
0
5
10
15
20
Time (s)

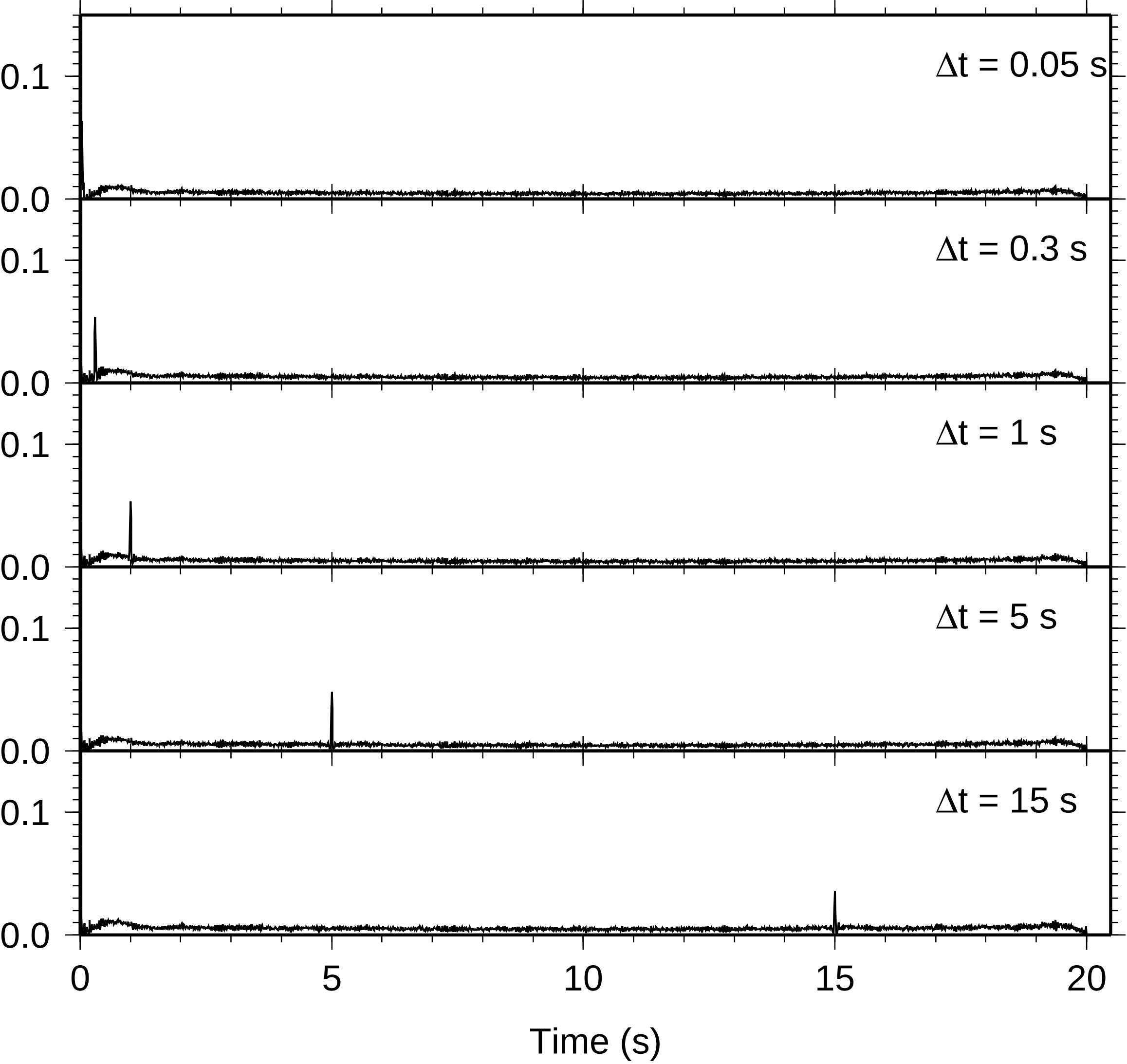
Δt = 0.05 s
Δt = 0.3 s
Δt = 1 s
Δt = 5 s
Δt = 15 s
0.1
0.0
0
5
10
15
20
Time (s)

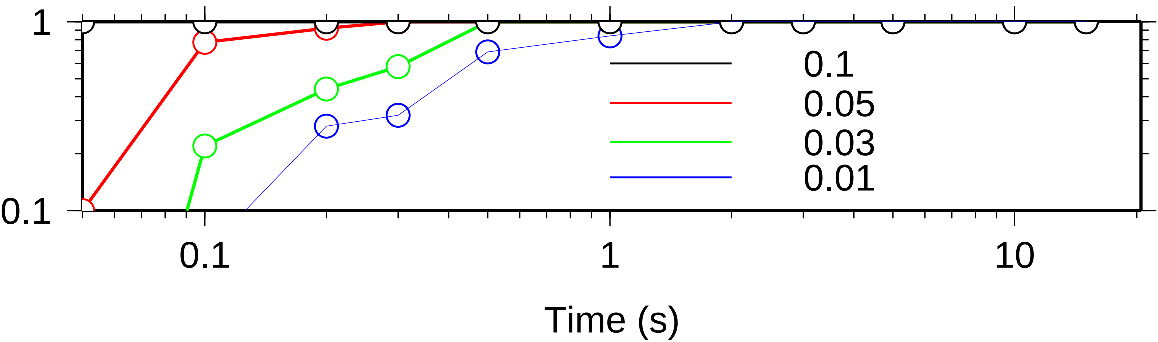
1
0.1
0.1
0.05
0.03
0.01
0.1
1
10
Time (s)

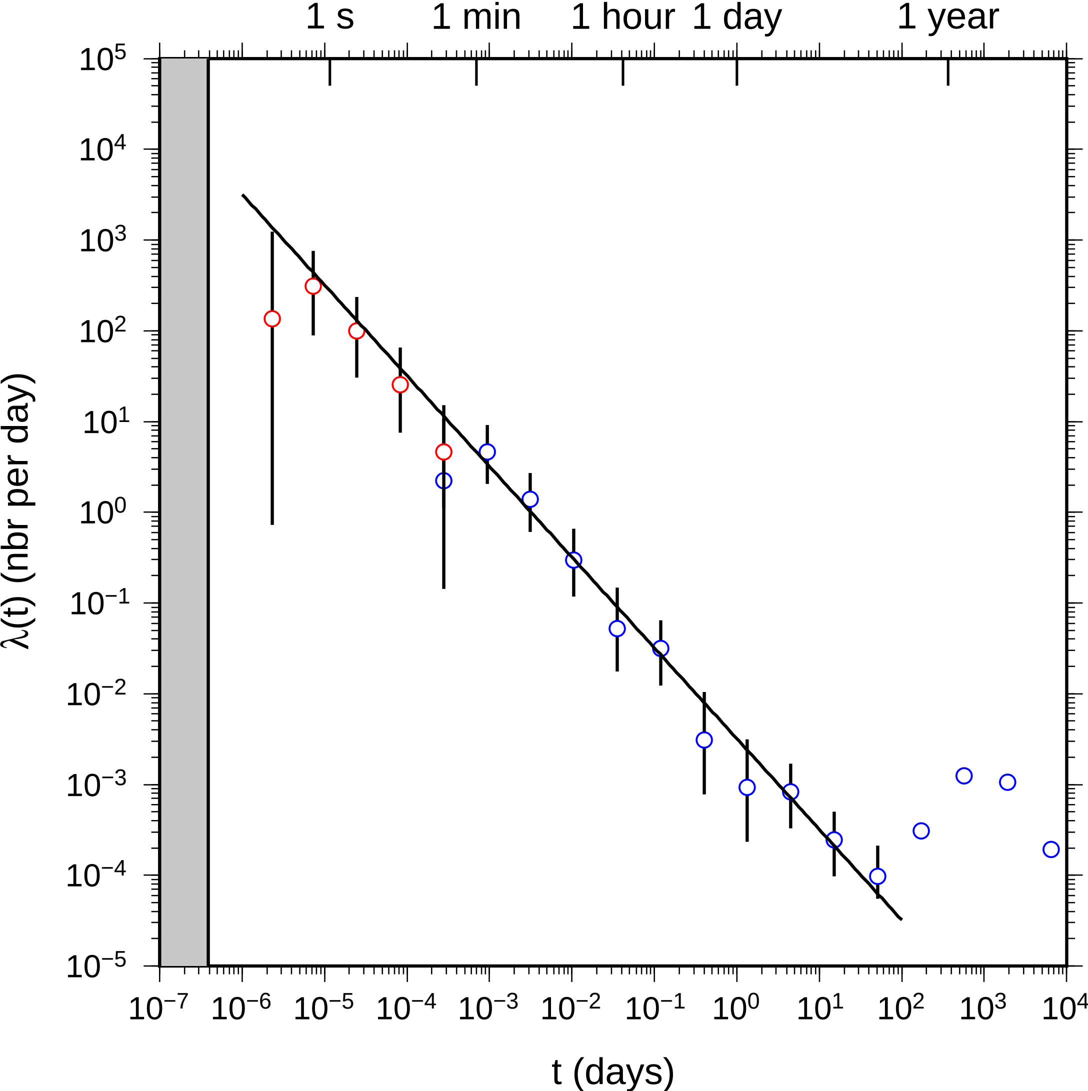
1 s
1 min
1 hour
1 day
1 year
10^5
10^4
10^3
10^2
10^1
10^0
10^{-1}
10^{-2}
10^{-3}
10^{-4}
10^{-5}
λ(t) (nbr per day)
10^{-7}
10^{-6}
10^{-5}
10^{-4}
10^{-3}
10^{-2}
10^{-1}
10^0
10^1
10^2
10^3
10^4
t (days)